Electronic Supplementary Information

Synthesis, Characterisation, and Magnetic Properties of a Permethylated Manganocene

Alexander Evans[a], Thomas A. Q. Arnold[a], Paul Ransom[a], Samantha C. Binding[a], William K. Myers[b], Agamemnon E. Crumpton[a], Zoë R. Turner[a], Jean-Charles Buffet[a], and Dermot O'Hare*[a]

[a]Chemistry Research Laboratory, Department of Chemistry, University of Oxford, 12 Mansfield Road, OX1 3TA Oxford, U.K.

[b] Centre for Advanced Electron Spin Resonance (CAESR), Inorganic Chemistry Laboratory, Department of Chemistry, University of Oxford, South Parks Road, Oxford, OX1 3QR, U.K. Chemistry

E-mail: dermot.ohare@chem.ox.ac.uk

1. EXPERIMENTAL

General methods and materials. Air and moisture-sensitive reactions were performed on a dual-manifold vacuum/N_2 line using standard Schlenk techniques, or in a N_2 filled MBraun Unilab glovebox. Hexane was dried using a Braun SPS-800 solvent purification system and stored over a K mirror. THF was dried at reflux over Na/benzophenone and distilled under N_2. THF was stored over activated 3 Å molecular sieves. Benzene-*d*$_6$ (99%) was obtained from Goss Scientific, dried over Na and freeze-pump-thaw degassed three times, before being vac transferred prior to use.

Solution NMR spectroscopy. NMR samples were prepared in the glovebox under N_2 atmosphere in Young's tap NMR tubes. ^1H and $^{13}C\{^1H\}$ NMR spectra were recorded on 300 MHz Varian VX-Works spectrometers. All chemical shifts were expressed as δ, in parts per million (ppm) relative to TMS (δ = 0). Solution phase Evans' method NMR samples were prepared in both benzene-d_6 and toluene-d_8 as above and were run on the 500 MHz Bruker AVIII 500 spectrometer.

Single Crystal X-Ray Diffraction. Crystals were mounted on MiTeGen MicroMounts using perfluoropolyether oil and rapidly transferred to either a SuperNova A or Synergy DW diffractometer fitted with an Oxford Cryostreams Cryostream open-flow nitrogen cooling device.[1] Data collections were carried out at low temperature, either 150 K or 100 K using Cu K_α radiation (l = 1.54178 Å) and data were processed using CrysAlisPro.[2] Structures were solved using charge flipping algorithm (SUPERFLIP)4 and refined on F^2 by full-matrix lest-squares regression using the Olex-2 software suite.[3] Using Olex2, the structures were solved with the SHELXT[4] structure solution program using Intrinsic Phasing and refined on F^2 with the SHELXL[5] refinement package using least squares minimisation. Geometric calculations were performed using PLATON,[6] and illustrations were created using ORTEP-3.[7] The crystal structure solution of Ind*H was refined as a two-component twin, implementing the twin-law (–1 0 0 | 0 –1 0 | 0 0 1) with BASF = 0.4569.

Ultraviolet–visible Spectroscopy. Optical measurement were conducted using UV-Vis-NIR spectrophotometer (PerkinElmer lambda 1050+). UV-Vis adsorption samples were prepared in the glovebox and were run in dry, degassed n-hexanes in a cuvette sealed with a Young's tap. Spectra between 250 and 800 nm.

Fourier-Transform Infrared Spectroscopy. FT-IR spectroscopy samples were prepared in the glovebox as discs using KBr that had been dried at 150 °C for eight hours under high vacuum. Discs were pressed in a custom-made barrel and sealed while run on a Nicolet iS5 ThermoScientific IR spectrometer.

SQUID magnetomery details The magnetic susceptibility data was measured on a powdered sample with a Quantum Design MPMS-5 SQUID magnetometer. The accurately weighed (26 mg) sample was placed in a gelatine capsule and loaded into a non-magnetic plastic straw before being lowered into the cryostat. Experimental susceptibility data was collected in a temperature range of 1.8-300 K under an applied field of 1000 G, and corrected for the underlying diamagnetism of $\chi_{dia} = -3.8376\times10^{-4}$ emu mol^{-1}, using Pascal's constants.[8]

EPR details. CW-EPR spectra were collected in the Centre for Advanced ESR (CAESR) in the Inorganic Chemistry Laboratory at the University of Oxford. X-band measurements performed with a Bruker-Biospin Micro EMX^{plus} spectrometer equipped with a PremiumX microwave bridge, a cylindrical TE$_{011}$-mode resonator (SHQE-W), an ESR-900 liquid helium cryostat, and an Oxford Instruments ITC-503s temperature controller. Custom simulation scripts for matrix diagonalization were written in MatLab^{TM}.

2. Synthesis and Characterisation

Updated ligand synthesis. The procedures are based upon a literature preparation.[9] Oxalyl chloride replaces thionyl chloride as the chlorinating agent and dichloromethane is introduced as the low boiling solvent, allowing the chlorination and Friedel-Crafts reactions to be combined in one pot. Methyllithium was found to be too basic to easily effect the ketone reduction and methylation and a softer cerium-based variant was introduced.[10-12] Iodine was succeeded by LiCl as the dehydrating agent, eliminating the need for column chromatography.[10]

Synthesis of 2,3,4,5,6,7-hexamethylindanone. 9.69 g (97 mmol, 1 eq.) trans-2-methylbutenoic acid was dissolved in 250 mL DCM and stirred under a flow of N_2 and 12.19 g (97 mmol, 1 eq.) oxalyl chloride added. A catalytic drop of DMF was added causing the reaction to effervesce vigorously and the reaction was stirred for 16 hours. The reaction vessel was cooled to <5 °C in an ice-bath and 13.16 g (98.5 mmol, 1.02 eq.) $AlCl_3$ was added. 12.3 g (92 mmol, 0.95 eq) 1,2,3,4-tetramethylbenzene was mixed with 25 mL DCM and was added in a slow dropwise manner, and the reaction mixture allowed to warm to room temperature, stirring, over four hours. 125 mL conc. HCl was mixed with 125 mL ice and was added to the reaction mixture, quenching it, before the DCM layer was decanted. The aqueous layer was extracted with two further portions of DCM and the combined organic phase washed with water, dried with $MgSO_4$, filtered, and removed in vacuo, affording the product as an off-white crystalline solid in 96 % yield (19 g, 88 mmol).

Synthesis of 1,2,3,4,5,6,7-heptamethylindan-1-ol. 20 g anhydrous $CeCl_3$ (81.1 mmol, 1.5 eq.) was activated by stirring in 300 mL dry, degassed THF under a nitrogen atmosphere for 16 h, before cooling to −78 °C. 47.3 mL methyllithium (1.6 M in Et_2O; 75.7 mmol, 1.4 eq.) was added fast dropwise to the white suspension turning it bright yellow. The solution was allowed to stir for a further hour warming to −35 °C before dropwise addition of 11.69 g 2,3,4,5,6,7-hexamethylindan-1-one (54.1 mmol, 1 eq.) in 100 mL THF, warming to room temperature and stirring for a further 12 h. The reaction mixture was quenched with 400 mL saturated aqueous ammonium chloride solution and was extracted in DCM (3 × 150 mL), dried over anhydrous $MgSO_4$ and reduced in vacuo affording a light brown oil. This oil was triturated with 2 mL hexane (4 °C), which was decanted after one hour affording an off-white crystalline solid in 96% yield (12.05 g, 51.9 mmol).

Synthesis of Ind*H. 9.21 g 1,2,3,4,5,6,7-heptamethylindan-1-ol (39.7 mmol, 1 eq.) was dissolved in 150 mL dry DMSO and allowed to stir under N_2. 2.53 g anhydrous lithium chloride (59.5 mmol, 1.5 eq) was quickly added to the pale brown solution, a reflux condenser was set up and the flask was heated to 110 °C and allowed to stir for 48 h, darkening in colour. Upon cessation of stirring, a dark brown immiscible layer can be seen to form which solidifies to a pale-yellow wax on cooling of the reaction mixture to room temperature. The product is extracted in pentane (3 × 150 mL), washed with distilled water (150 mL), dried over anhydrous $MgSO_4$ and removed under reduced pressure affording a pale brown crystalline solid in 92% yield (7.85 g, 36.6 mmol).

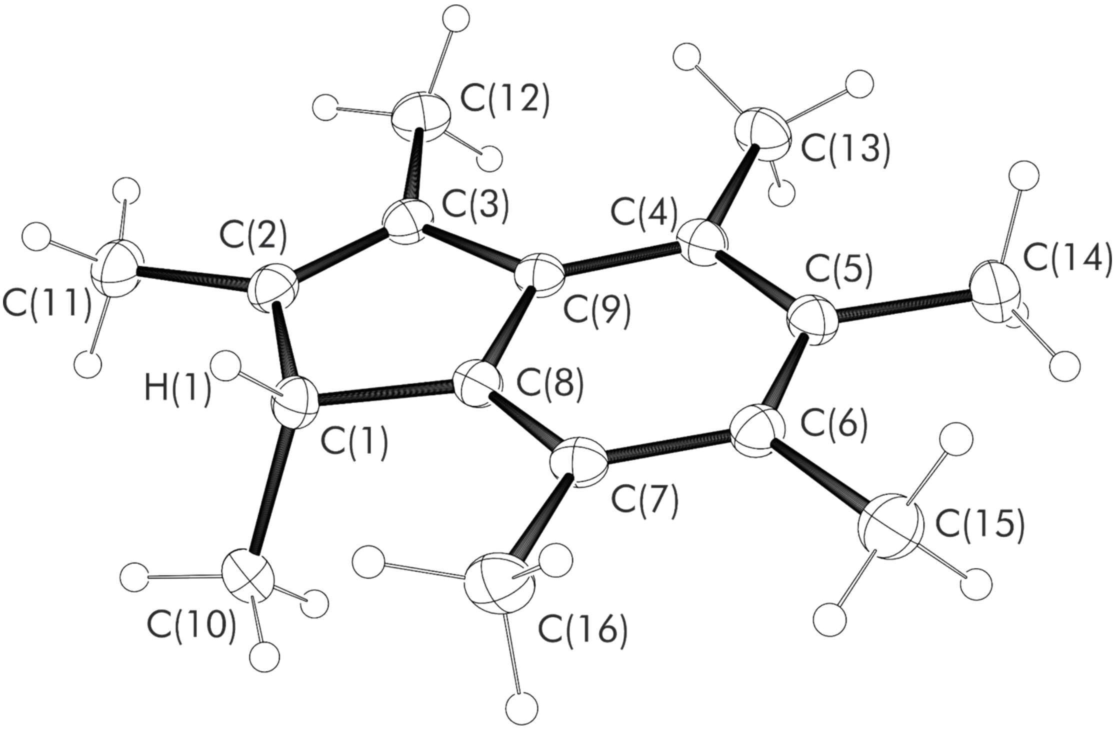

Figure S1 Molecular structure of Ind* (displacement ellipsoids are drawn at 30% probability). Selected distance, C_6-C_5 1.407(2) Å

Table S1 Selected experimental crystallographic data for Ind*H.

Chemical formula	$C_{16}H_{22}$
M_r	214.33
Crystal system, space group	Monoclinic, $P2_1/c$
Temperature (K)	150
a, *b*, *c* (Å)	13.0353 (4), 10.9285 (4), 9.0453 (3)
β (°)	91.765 (3)
V (Å^3)	1287.95 (7)
Z	4
Radiation type	Cu *K*α
μ (mm^{-1})	0.45
Crystal size (mm)	0.22 × 0.12 × 0.08
Diffractometer	SuperNova, Dual, Cu at home/near, Atlas
Absorption correction	Multi-scan *CrysAlis PRO* 1.171.42.72a (Rigaku Oxford Diffraction, 2022) Empirical absorption correction using spherical harmonics, implemented in SCALE3 ABSPACK scaling algorithm.
T_{min}, T_{max}	0.834, 1.000
No. of measured, independent and observed [$I > 2\sigma(I)$] reflections	5161, 5161, 4125
$(\sin \theta/\lambda)_{max}$ (Å^{-1})	0.630
$R[F^2 > 2\sigma(F^2)]$, $wR(F^2)$, S	0.047, 0.143, 1.09
No. of reflections	5161
No. of parameters	153
H-atom treatment	H-atom parameters constrained
$\Delta\rho_{max}$, $\Delta\rho_{min}$ (e Å^{-3})	0.25, −0.23
CCDC Deposition Number	2421030

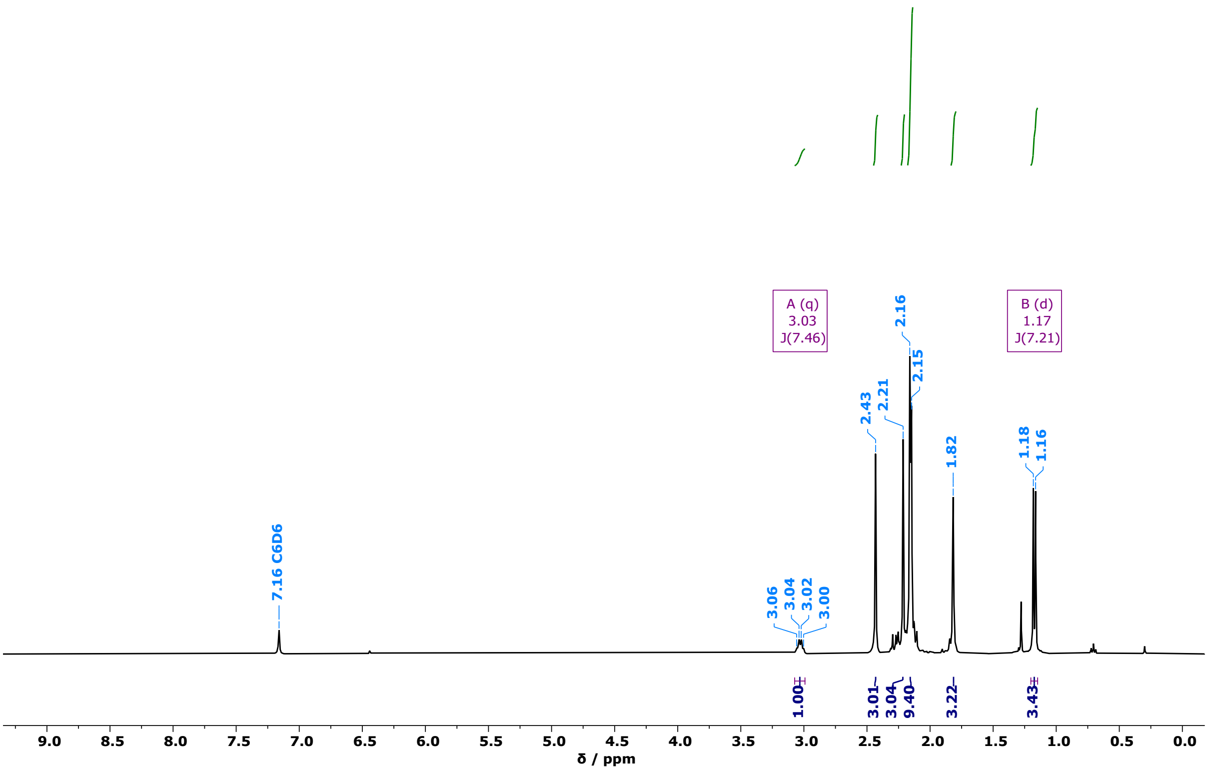

Figure S2 ^{1}H NMR Ind*(Benzene-*d*$_6$, 298 K, 400 MHz).

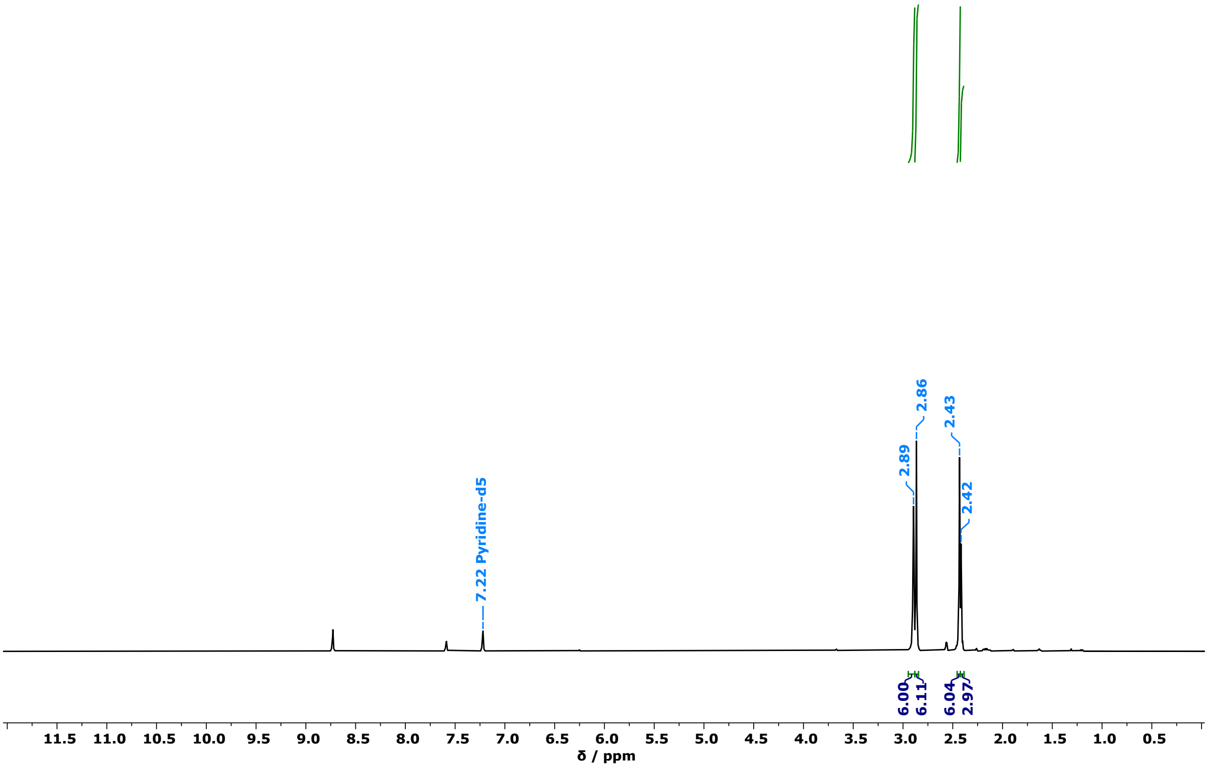

Figure S3^{1}H NMR Ind*(Pyridine-*d*$_5$, 298 K, 400 MHz).

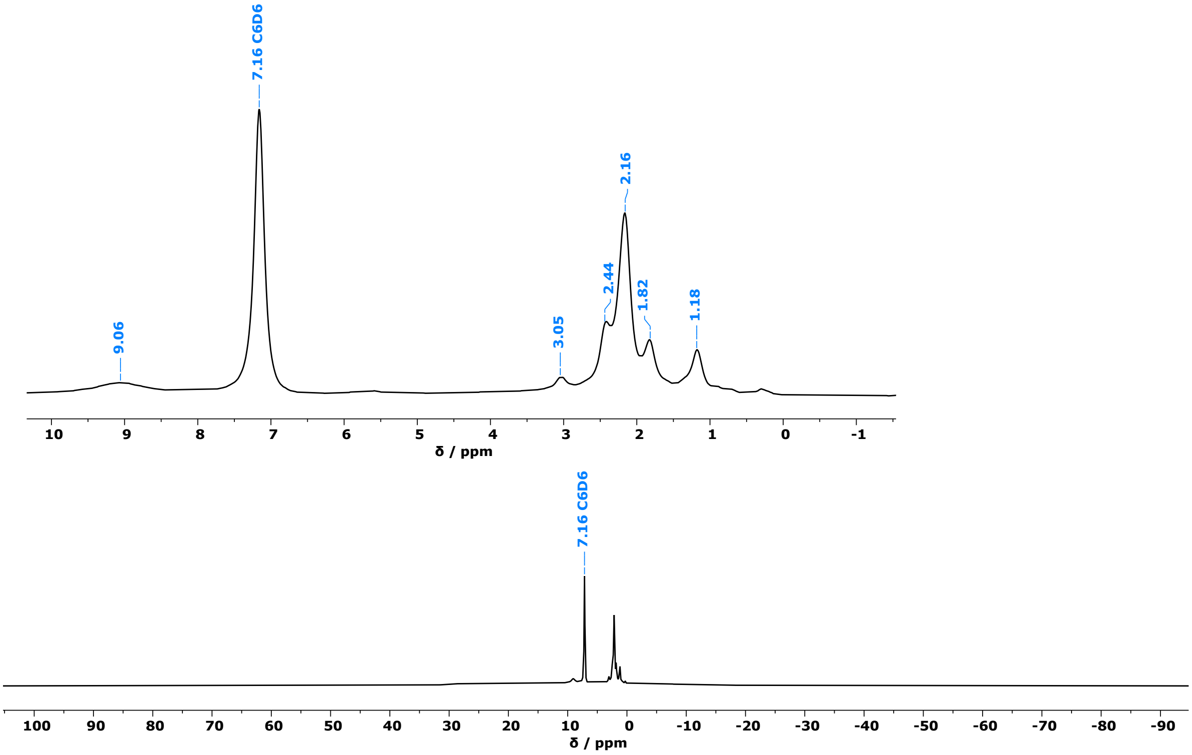

Figure S4 ^{1}H NMR full spectra of Ind*$_2$Mn and insert is of relevant region (Benzene-d_6, 298 K, 500 MHz).

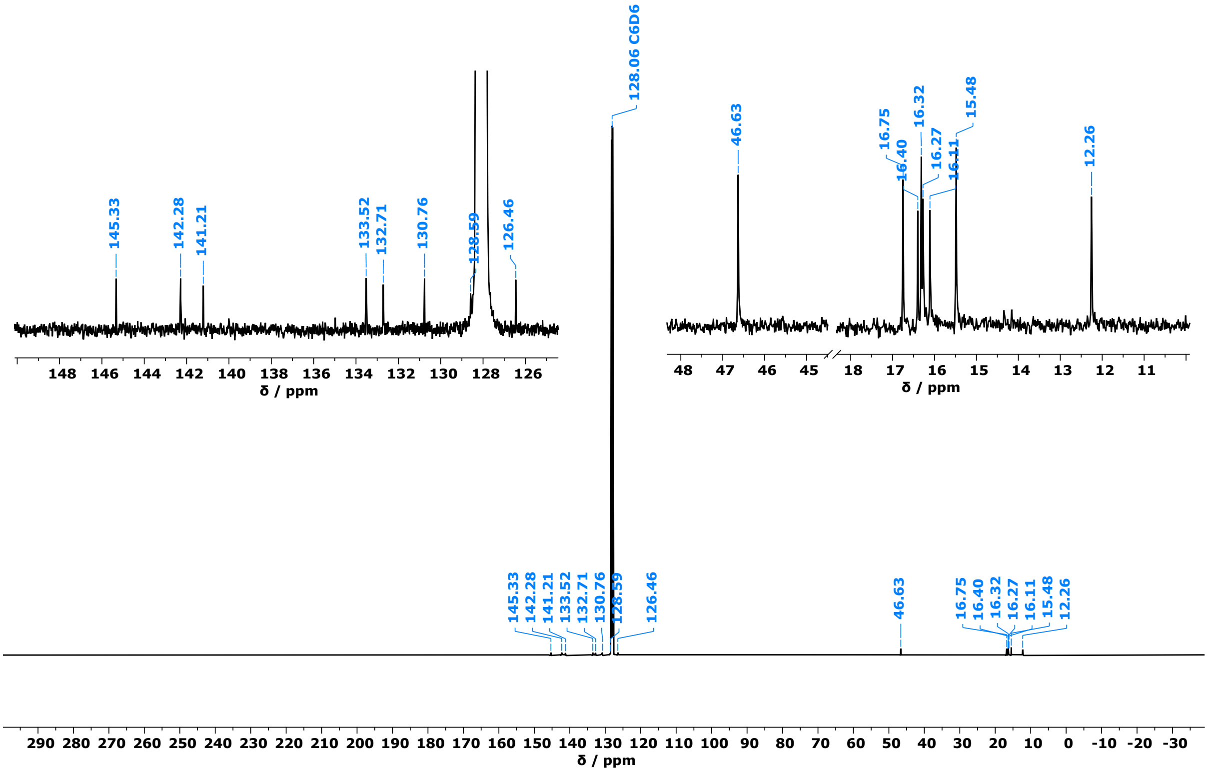

Figure S5 $^{13}C\{^{1}H\}$ NMR full spectra of Ind*$_2$Mn and inserts are of relevant regions (benzene-d_6, 298 K, 499.9 MHz).

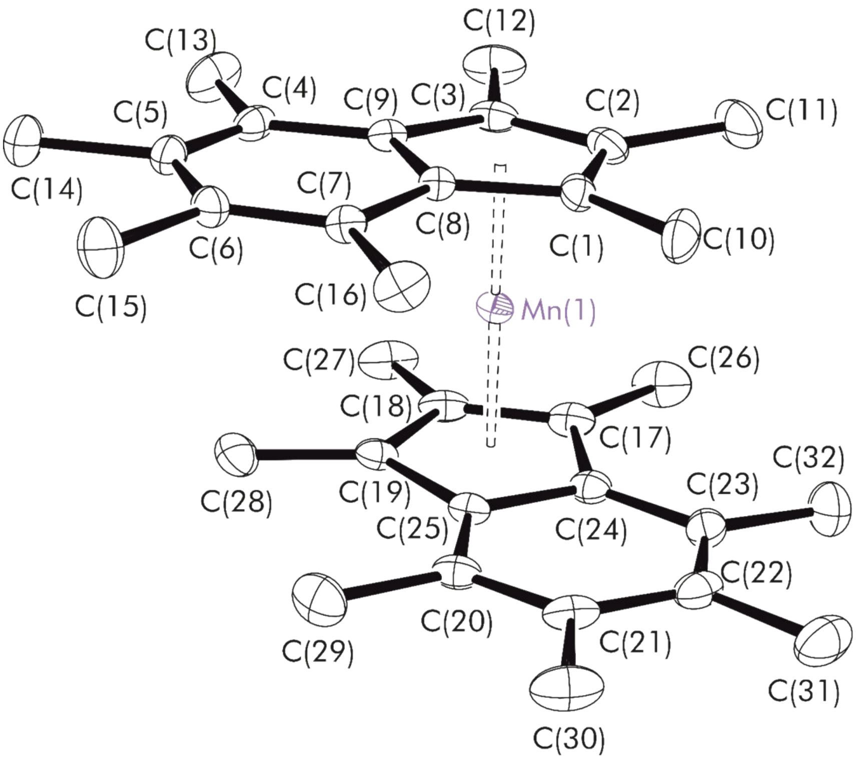

Figure S6 Fully labelled molecular structure of $(Ind^*)_2Mn$. For clarity, hydrogens atoms were omitted (displacement ellipsoids are drawn at 30% probability).

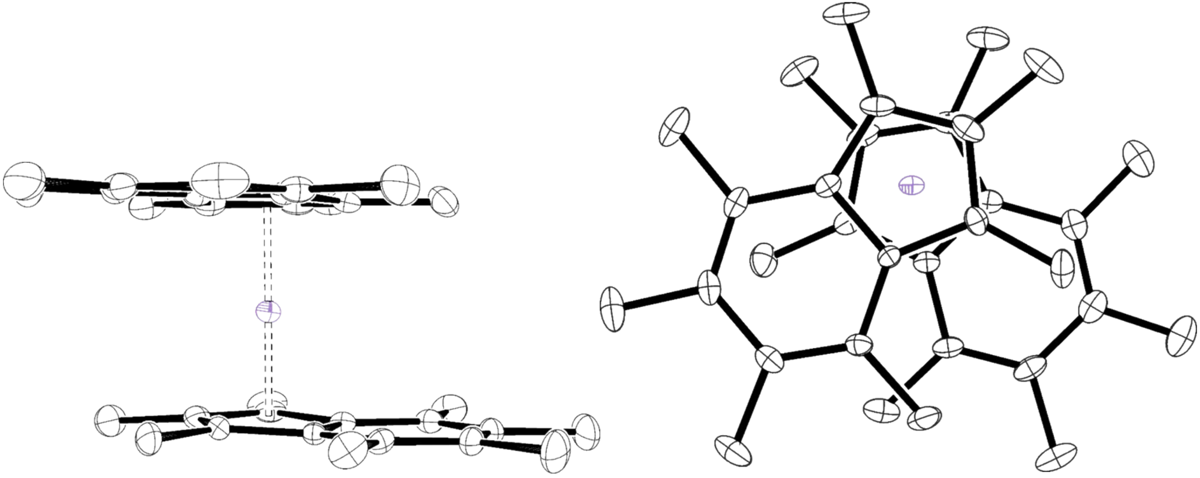

Figure S7 Alternate views of the molecular structure of $(Ind^*)_2Mn$. For clarity, hydrogens atoms were omitted (displacement ellipsoids are drawn at 30% probability).

Table S2 Selected bond lengths (Å) and angles (°) for Ind^*_2Mn.

$M\text{-}C_{avg}$	2.127
$Cp_{cent}\text{-}M$	1.7400(6)
$\Delta_{M\text{-}C}$	0.073, 0.073
RA	85.2(2)
$C_6\text{-}C_5$	1.443(2)
$C_{21}\text{-}C_{22}$	1.441(2)

Definitions of structural parameters. The rotation angle (RA) and indeed torsion angles all measure the twist of the two indenyl rings relative to one another with 0° being eclipsed and 180° being staggered. However, these parameters are calculated in different ways but in this work RA is based on the torsion angle first introduced by Calhorda *et al.* [C(2)-Cp_{cent}-Cp_{cent}-C(18)] and adapted for Ind^*_2Mn: [C(11)-C(2)-C(18)-C(27)].[13] $\Delta_{M\text{-}C}$, also termed the ring-slip parameter is a measure of how far the metal distorts from η^5- bonding towards η^3- and is a reasonable quantifier of the "indenyl effect". It is measured in angstroms and calculated according to Equation S1.

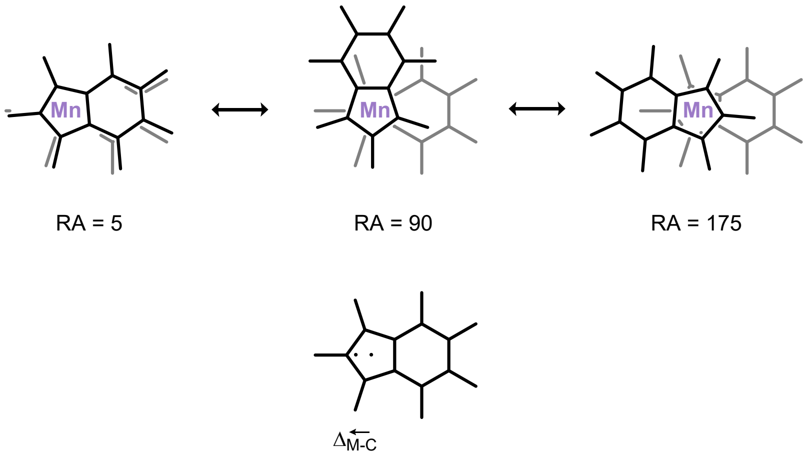

Figure S8 Visually defined structural parameters.

$$\Delta_{M-C} = \left\{\frac{C(8) + C(9)}{2}\right\} - \left\{\frac{C(1) + C(1) + C(3)}{3}\right\}$$

Equation S1 Definition of $\Delta_{M\text{-}C}$.

Table S3 Selected experimental crystallographic data for Ind^*_2Mn.

Chemical formula	$C_{32}H_{42}Mn$
M_r	481.59
Crystal system, space group	Triclinic, *P*-1
Temperature (K)	100
a, *b*, *c* (Å)	9.0512 (1), 10.4398 (1), 15.8124 (1)
α, β, γ (°)	73.273 (1), 84.778 (1), 63.915 (1)
V (Å^3)	1284.09 (2)
Z	2
Radiation type	Cu *K*α
μ (mm^{-1})	4.28
Crystal size (mm)	0.3 × 0.13 × 0.04

Diffractometer	XtaLAB Synergy R, DW system, HyPix-Arc 150
Absorption correction	Multi-scan *CrysAlis PRO* 1.171.42.49 (Rigaku Oxford Diffraction, 2022) Empirical absorption correction using spherical harmonics, implemented in SCALE3 ABSPACK scaling algorithm.
T_{min}, T_{max}	0.548, 1.000
No. of measured, independent and observed [$I > 2\sigma(I)$] reflections	48167, 5238, 5064
R_{int}	0.028
$(\sin \theta/\lambda)_{max}$ (Å^{-1})	0.629
$R[F^2 > 2\sigma(F^2)]$, $wR(F^2)$, S	0.029, 0.081, 1.08
No. of reflections	5238
No. of parameters	312
H-atom treatment	H-atom parameters constrained
$\Delta\rho_{max}$, $\Delta\rho_{min}$ (e Å^{-3})	0.27, −0.34
CCDC Deposition Number	2421029

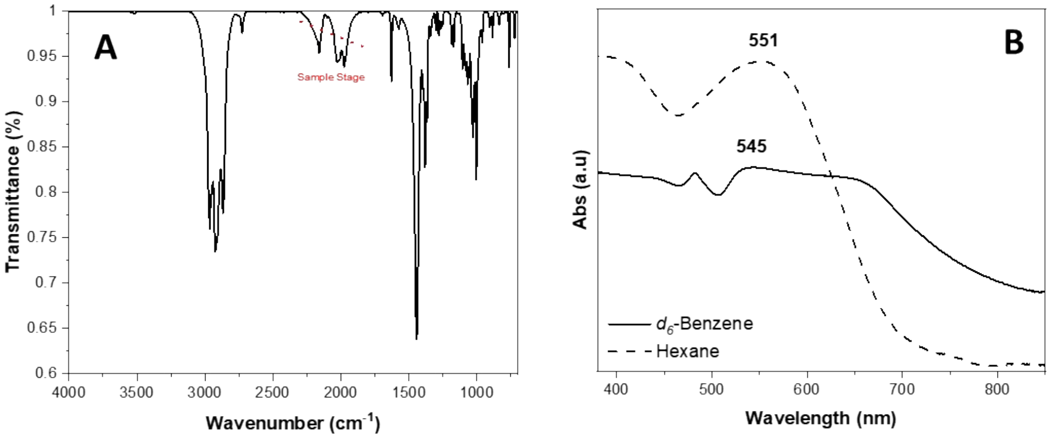

Figure S9 (**A**) FT-IR and (**B**) UV-Vis of $(Ind^*)_2Mn$.

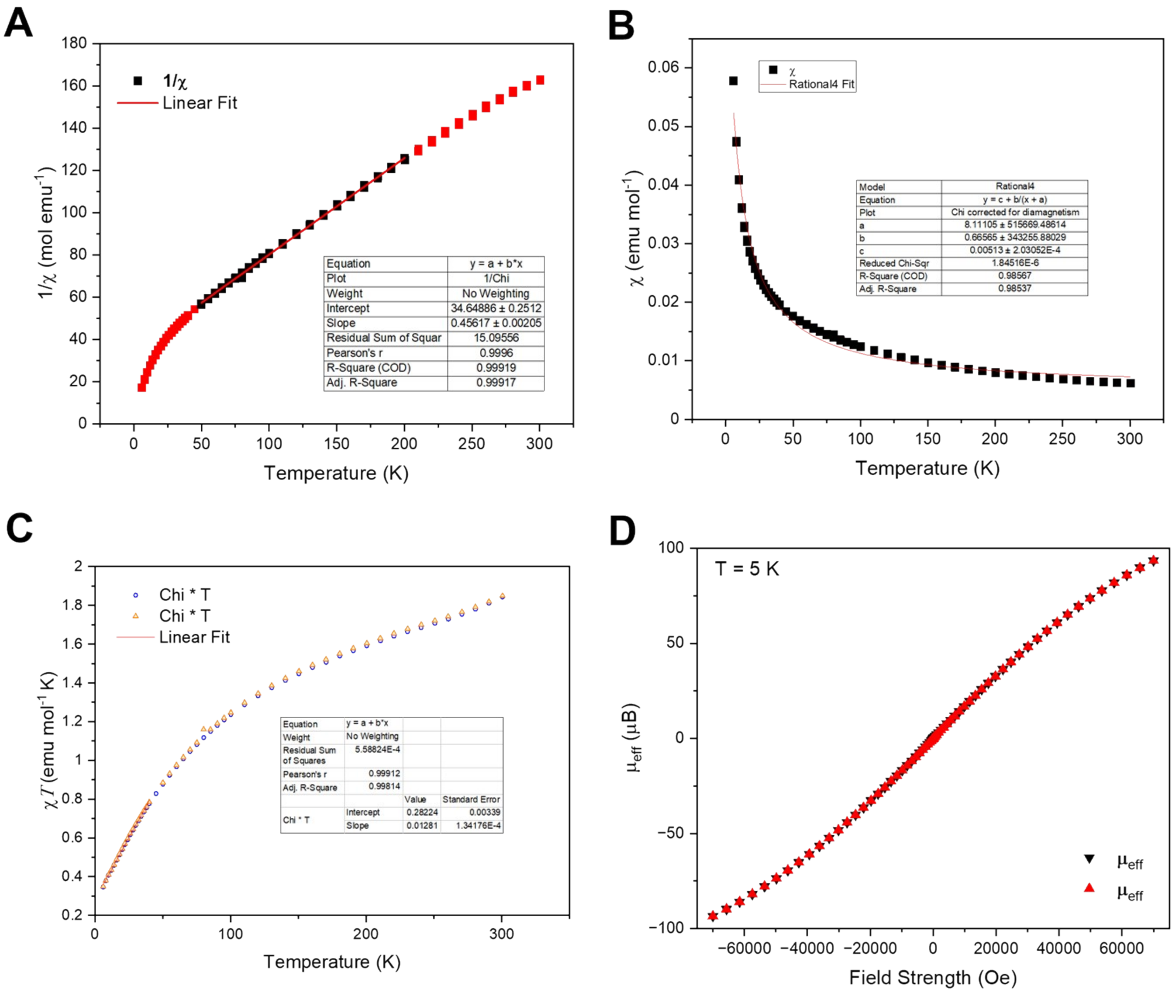

Equation	y = a + b*x
Plot	1/Chi
Weight	No Weighting
Intercept	34.64886 ± 0.2512
Slope	0.45617 ± 0.00205
Residual Sum of Squar	15.09556
Pearson's r	0.9996
R-Square (COD)	0.99919
Adj. R-Square	0.99917

Model	Rational4
Equation	y = c + b/(x + a)
Plot	Chi corrected for diamagnetism
a	8.11105 ± 515669.48614
b	0.66565 ± 343255.88029
c	0.00513 ± 2.03052E-4
Reduced Chi-Sqr	1.84516E-6
R-Square (COD)	0.98567
Adj. R-Square	0.98537

Equation	y = a + b*x		
Weight	No Weighting		
Residual Sum of Squares	5.58824E-4		
Pearson's r	0.99912		
Adj. R-Square	0.99814		
		Value	Standard Error
Chi * T	Intercept	0.28224	0.00339
	Slope	0.01281	1.34176E-4

Figure S10 SQUID magnetronomy plots: (**A**) linear fit of 1/χ between 50-200 K calculated Weiss constant, θ = –44 K. Calculated f_{HS}: $\mu_{eff,exp}^2 = f_{HS} \cdot \mu_{eff,HS}^2 + f_{LS} \cdot \mu_{eff,LS}^2$. $(3.85)^2 = f_{HS}(5.92)^2 + (1 - f_{HS})(1.88)^2$. $f_{HS} \approx 0.358$;[14] (**B**) χ *vs* T, (**C**) χT *vs* T, and (**D**) a hysteresis loop (T = 5 K) classically describe a paramagnetic system.

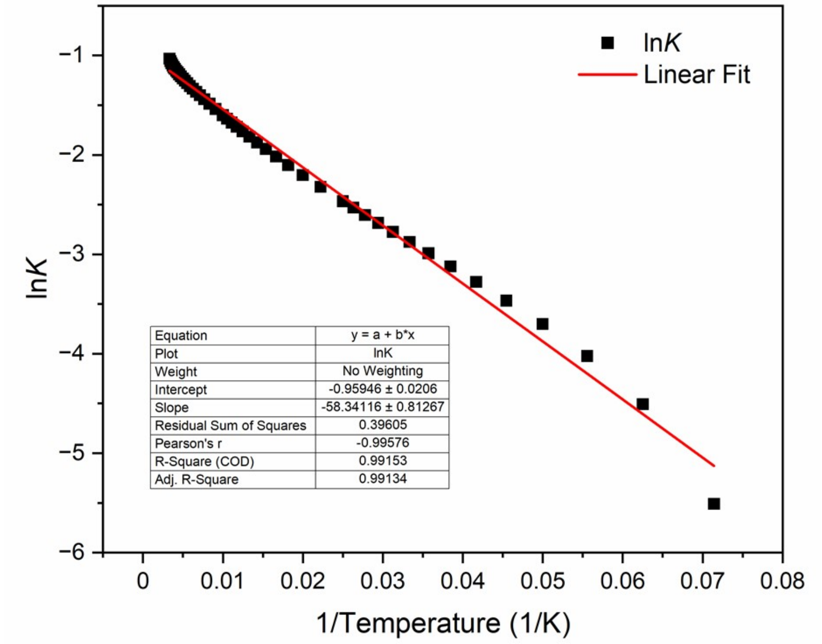

Equation	y = a + b*x
Plot	lnK
Weight	No Weighting
Intercept	-0.95946 ± 0.0206
Slope	-58.34116 ± 0.81267
Residual Sum of Squares	0.39605
Pearson's r	-0.99576
R-Square (COD)	0.99153
Adj. R-Square	0.99134

Figure S11 ln*K* *vs* T^{-1} plot for high-spin, low-spin equilibrium for $(Ind^*)_2Mn$ determined by solid-state magnetic susceptibility. $R^2 = 0.992$, $\Delta H = 0.485 \pm 0.007$ kJ mol^{-1}, and $\Delta S = -7.98 \pm 0.17$ J mol^{-1} .[15]

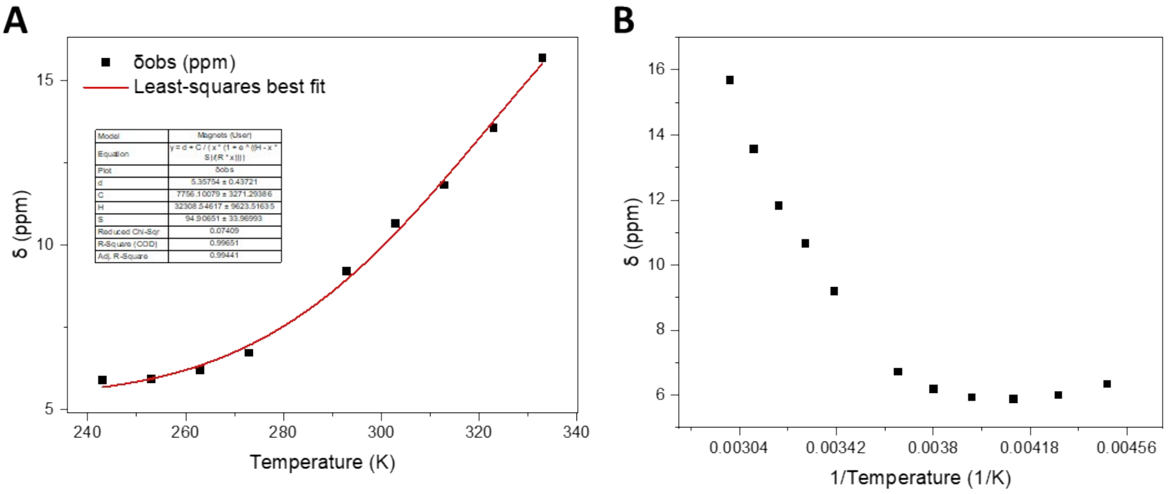

Model	Magnets (User)
Equation	y = d + C / (x * (1 + e ^ ((H - x * S)/(R * x))))
Plot	δobs
d	5.35754 ± 0.43721
C	7756.10079 ± 3271.29386
H	32308.54617 ± 9623.51635
S	94.90651 ± 33.96993
Reduced Chi-Sqr	0.07409
R-Square (COD)	0.99651
Adj. R-Square	0.99441

Figure S12 (**A**) Temperature variation and (**B**) reciprocal temperature variation of the ^1H NMR chemical shift for the resonance of the wing-tip methyl group between 243 K and 333 K (Me_2 in Figure 2) for $(Ind^*)_2Mn$. Black squares represent experimental data and the red line is the least-squares best fit to $\delta_{obs} = \delta_{LS} + \dfrac{C}{T[1 + e^{(\Delta H - T\Delta S/RT)}]}$.[10, 16, 17] $R^2 = 0.997$, $\Delta H = 32 \pm 9$ kJ mol^{-1}, $\Delta S = 90 \pm 30$ J mol^{-1}, $C = 7000 \pm 3000$ K, and $f_{HS} = 17\%$ at 300 K, $f_{HS} = [HS]/[LS]$. The chemical shift measurements at 233 and 223 K are not included in this analysis, as they indicate an increasing shift upon decreasing temperature, which cannot be accounted for in the above model. This behaviour is most likely explained by a temperature dependence of the ^1H NMR shift of Me_2 due to the paramagnetic nature of the low spin complex. The result is a deviation from the above model, and correspondingly high errors in the derived thermodynamic parameters.

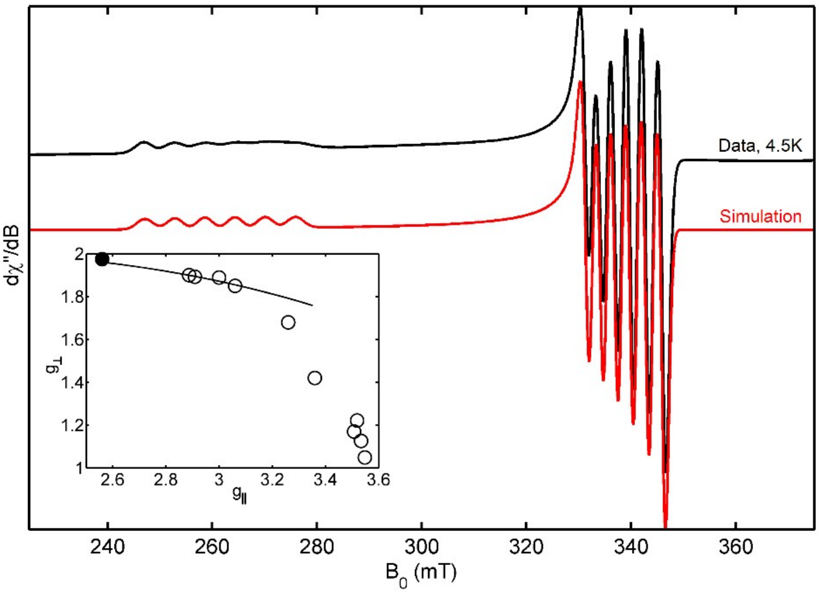

Figure S13 X-band EPR simulation of the low-spin species of (Ind*)$_2$Mn for data collected at 4.5 K. Simulation parameter values are $g_{||}$ = 2.56 and $g_{\perp}$ = 1.975, $A_{||}$(^{55}Mn) = 206 MHz and $A_{\perp}$(^{55}Mn) = 80 MHz. *Inset*: parametric plot of literature g-values for low-spin Mn(II) sandwich compounds with this work in solid dot.[18] The inset line represents variation of the axial symmetry distortion parameter, *δ*, in equations 1a-c. Acquisition conditions were as stated in the main text.

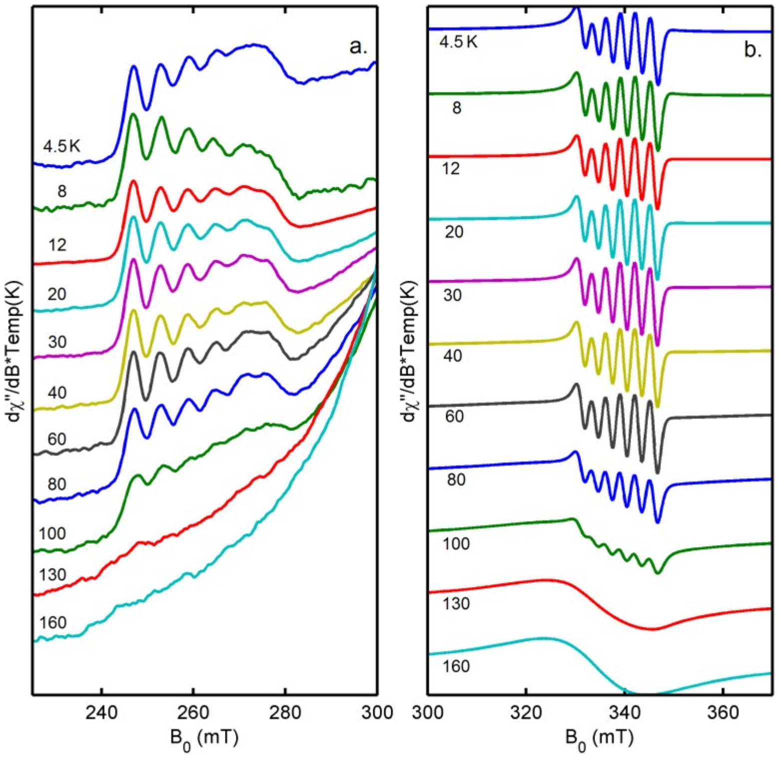

Figure S14 Temperature dependence of individual components of the low-spin signal in the transition to a high-spin signal. In the g|| region, 4.5 K and 8 K data represent acquisitions following a re-freezing of the sample, while the small decrease in the 12 K intensity is due to slight saturation at that temperature. Acquisition conditions were as stated in the main text.

Computational Details

General computation details. All calculations were performed using the ORCA software suite unless otherwise specified.[19] A range of functionals were used to probe the ΔE¬HL for the crystal structure geometry, all utilizing the def2-TZVP basis set.[20, 21] Specifically, we examined the following functionals: B3LYP,[22-25] R2SCAN,[26] M062X,[27] WB97X,[28] BP86,[29] PBE,[30] PBE0,[31] MN15L,[32] M06L,[33] M05,[33] M052X,[34] MN15,[35] TPSSH,[36] TPSS0,[36] M06, r2SCANh,[26] and OLYP.[37] The functionals and their corresponding ΔE values are shown in **Table S4**.

Table S4 Functionals

	Crystal structure (kcal mol^{-1})
CCSD(T)	32.00623
CASSCF	27.633
MN15	33.39701

Functional	ΔE (kcal mol^{-1})
BP86	-52.7907
PBE	-52.744
TPSSh	-45.242
OLYP	-40.9621
WB97X	-37.826
B3LYP	-37.6495
R2SCAN	-37.0324
r2scan-3c	-36.508
wb97x-3c	-30.9477
r2SCANh	-28.4273
PBE0	-27.9945
pbeh-3c	-11.1639
M062X	-5.11955
M062X	5.119578
M052X	8.982872
MN15L	14.12748
M06	15.38958
M05	18.09392
TPSS0	30.55783
M06L	31.56466
MN15	33.39701
TPSSH	45.24218

We found that MN15 provided the best match with the CCSD(T) calculations detailed below. Geometry optimizations were performed on both the high and low spin electronic configurations, along with scanning the RA angle for both the high and low energy configurations. Single-point calculations were performed with the CCSD(T) procedure outlined below.

CCSD(T)-DLPNO. The coupled cluster single, double, and perturbative triple excitation (DLPNO-CCSD(T)) calculations were carried out using the BP86 functional to generate reference orbitals.[38-47] This functional has been shown to provide reliable results for spin-splitting energetics and ground state predictions, as highlighted in reference [31]. The cc-pVDZ basis set[48] was used, with cc-pVTZ/C employed for correlated calculations to achieve better accuracy. VeryTightSCF thresholds were applied to ensure complete convergence of the self-consistent field (SCF) procedure, along with NormalPNO threshold, which provides a cost-effective balance between computational efficiency and accuracy.

The choice of BP86 orbitals was guided by literature precedence, which highlights their superiority in spin-state energetics and agreement with canonical CCSD(T) methods. For example, studies have shown that BP86 orbitals correctly predict the ground state for systems and offer mean deviations within 4 kcal/mol relative to canonical CCSD(T). These orbitals also exhibit an optimal balance in the number of pair natural orbitals (PNOs), as detailed in supplementary materials of prior studies.[49]

CASSCF/NEVPT. Complete active space self-consistent field (CASSCF) calculations followed by *N*-electron valence perturbation theory (NEVPT2) corrections were performed.[47, 50-52] The active space comprised 9 electrons in 12 orbitals, including 2 bonding orbitals, 5 metal-centred d orbitals, and 5 3 d’ double-shell orbitals. This choice of active space is supported by previous studies, which demonstrate that inclusion of the d’ double-shell orbitals enhance accuracy for systems of this type. The def2-TZVP basis set was employed for all atoms, with def2-TZVP/C used for correlated calculations.

Table S5 Orbital occupancy of CASSCF/NEVPT active space

Orbital Number	Occupancy	eH	eV
126	1.7975	-0.306212	-8.3325
127	1.7441	-0.277597	-7.5538
128	1.3899	-0.187782	-5.1098
129	1.3158	-0.168846	-4.5945
130	1.1748	-0.112336	-3.0568
131	0.7016	0.089904	2.4464
132	0.6009	0.106506	2.8982
133	0.1847	0.191967	5.2237
134	0.0301	0.551555	15.0086
135	0.0290	0.586597	15.9621
136	0.0235	0.703114	19.1327
137	0.0081	1.119556	30.4647

Table S6 Density matrix of CASSCF/NEVPT active space.

	1	**2**	**3**	**4**	**5**	**6**	**7**	**8**	**9**	**10**	**11**	**12**
1	1.797502	1.00E-06	2.00E-06	-1.00E-06	0	1.00E-06	-5.00E-06	0	0	0	-1.00E-06	0
2	1.00E-06	1.744138	1.00E-06	-1.00E-06	-1.00E-06	-2.00E-06	-1.00E-06	0	1.00E-06	0	0	-1.00E-06
3	2.00E-06	1.00E-06	1.389855	2.40E-05	-4.00E-06	1.00E-06	-1.00E-06	0	0	-4.00E-06	0	0
4	-1.00E-06	-1.00E-06	2.40E-05	1.315782	-1.20E-05	0	0	4.00E-06	1.00E-06	-2.00E-06	-1.00E-06	0
5	0	-1.00E-06	-4.00E-06	-1.20E-05	1.174842	1.00E-06	0	1.00E-06	-2.00E-06	0	-1.00E-06	0
6	1.00E-06	-2.00E-06	1.00E-06	0	1.00E-06	0.701563	-1.10E-05	-1.00E-06	-1.00E-06	0	0	1.00E-06
7	-5.00E-06	-1.00E-06	-1.00E-06	0	0	-1.10E-05	0.600895	-7.00E-06	0	-2.00E-06	0	0
8	0	0	0	4.00E-06	1.00E-06	-1.00E-06	-7.00E-06	0.184731	0	0	0	0
9	0	1.00E-06	0	1.00E-06	-2.00E-06	-1.00E-06	0	0	0.030124	0	0	0
10	0	0	-4.00E-06	-2.00E-06	0	0	-2.00E-06	0	0	0.028982	0	0
11	-1.00E-06	0	0	-1.00E-06	-1.00E-06	0	0	0	0	0	0.023499	0
12	0	-1.00E-06	0	0	0	1.00E-06	0	0	0	0	0	0.008088

Orbital 126 Orbital 127 Orbital 128 Orbital 129

Orbital 130 Orbital 131 Orbital 132 Orbital 133

Orbital 134 (two viewpoints) Orbital 135 (two viewpoints)

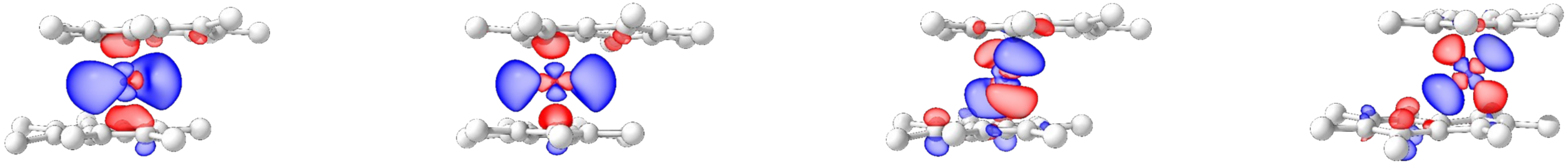

Orbital 136 (two viewpoints) Orbital 137 (two viewpoints)

Figure S15 Active space comprising 9 electrons in 12 orbitals, including 2 bonding orbitals, 5 metal-centred d orbitals, and 5 3 d' double-shell orbitals.

EDA. Energy decomposition analysis (EDA) was performed to gain insight into the bonding interactions within the studied systems, comparing the Ind* system with that of the Cp* ligand system. The initial decomposition analysis was conducted using the sobEDA method[53] with the Gaussian 16.C program[54] and Multiwfn,[55, 56] employing the MN15 functional and the def2-TZVP basis set, consistent with the ORCA setup. Further decomposition of the E_{orb} term was carried out using the EDA-NOCV method[57, 58] in ORCA, allowing for detailed examination of pairwise deformation densities.

Figures. All molecular graphics and visualisations were generated using ChimeraX 1.9.[59] This software was employed to create high-quality figures that effectively represent the geometric and electronic properties of the systems studied.

Table S7 sobEDA energy partitioning.[a]

Ligand	Cp*	I*
Total interaction energy	-734.76	-717.47
Physical components of interaction energy derived by sobEDA		
Electrostatic (E_{els})	-1020.16	-1012.13
Exchange (E_x)	-80.59	-79.02
Pauli repulsion (E_{eep})	605.69	767.52
Exchange-repulsion ($E_{xrep} = E_x + E_{rep}$)	525.1	688.5
Orbital (E_{orb})	-605.69	-767.52
DFT correlation (E_{DFTc})	-76.03	-79.88
Dispersion correction (E_{dc})	0	0
Coulomb correlation ($E_c = E_{DFTc} + E_{dc}$)	-76.03	-79.88

[a] Units in kcal mol^{-1}.

Table S8 EDA-NOCV pair densities.

	I*			Cp*		
	α	β	Σ	α	β	Σ
E_{orb}	-324.3	-331.37	-655.67	-343.46	-349.56	-693.01
pair1	-181.61	-169.4	-351.01	-138.8	-167.33	-306.13
pair2	-62.71	-71.48	-134.19	-132.6	-102.94	-235.54
pair3	-19.04	-46.82	-65.86	-35.23	-20.2	-55.43
pair4	-17.63	-6.66	-24.29	-9.05	-10.86	-19.91

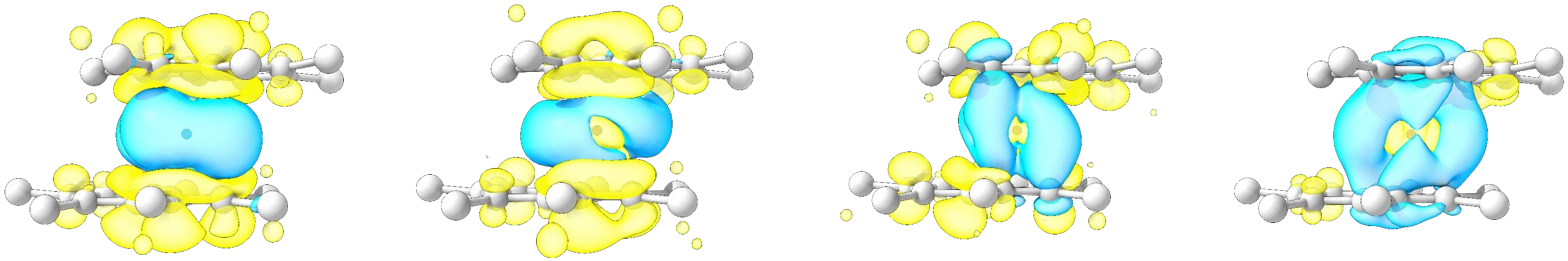

Ind* pair 1 Ind* pair 2 Ind* pair 3 Ind* pair 4

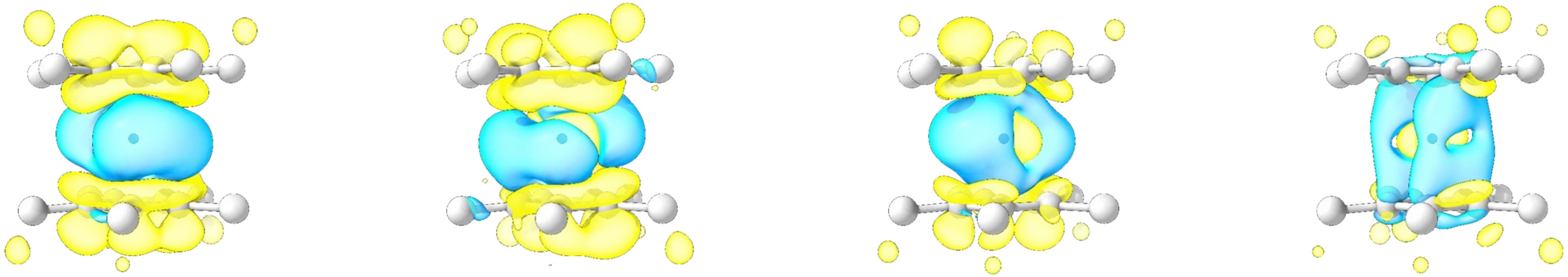

Cp* pair 1 Cp* pair 2 Cp* pair 3 Cp* pair 4

Figure S16 Pairwise deformation densities of Cp* and Ind*.

REFERENCES

1. J. Cosier and A. M. Glazer, *J. Appl. Crystallogr.*, 1986, **19**, 105–107.
2. CrysAlisPRO, Oxford Diffraction /Agilent Technologies UK Ltd, Yarnton, England.
3. O. V. Dolomanov, L. J. Bourhis, R. J. Gildea, J. A. K. Howard and H. Puschmann, *J. Appl. Cryst.*, 2009, **42**, 339–341.
4. G. Sheldrick, *Acta Crystallogr. Sect. A*, 2015, **71**, 3–8.
5. G. Sheldrick, *Acta Crystallogr. Sect. C*, 2015, **71**, 3–8.
6. A. Spek, *J. Appl. Crystallogr.*, 2003, **36**, 7–13.
7. L. J. Farrugia, *J. Appl. Crystallogr.*, 1997, **30**, 565–565.
8. G. A. Bain and J. F. Berry, *J. Chem. Educ.*, 2008, **85**, 532.
9. D. O'Hare, J. C. Green, T. Marder, S. Collins, G. Stringer, A. K. Kakkar, N. Kaltsoyannis, A. Kuhn and R. Lewis, *Organometallics*, 1992, **11**, 48–55.
10. A. E. Ashley, A. R. Cowley and D. O'Hare, *Eur. J. Org. Chem.*, 2007, **2007**, 2239–2242.
11. T. Imamoto, N. Takiyama, K. Nakamura, T. Hatajima and Y. Kamiya, *J. Am. Chem. Soc.*, 1989, **111**, 4392–4398.
12. T. Imamoto, Y. Sugiura and N. Takiyama, *Tet. Lett.*, 1984, **25**, 4233–4236.
13. M. J. Calhorda, V. Félix and L. s. F. Veiros, *Coord. Chem. Rev.*, 2002, **230**, 49–64.
14. M. E. Switzer, R. Wang, M. F. Rettig and A. H. Maki, *J. Am. Chem. Soc.*, 1974, **96**, 7669–7674.
15. M. D. Walter, C. D. Sofield, C. H. Booth and R. A. Andersen, *Organometallics*, 2009, **28**, 2005–2019.
16. W. L. Olson, A. M. Stacy and L. F. Dahl, *J. Am. Chem. Soc.*, 1986, **108**, 7646–7656.
17. M. E. Smith and R. A. Andersen, *J. Am. Chem. Soc.*, 1996, **118**, 11119–11128.
18. J. L. Robbins, N. M. Edelstein, S. R. Cooper and J. C. Smart, *J. Am. Chem. Soc.*, 1979, **101**, 3853–3857.
19. F. Neese, *Wiley Interdiscip. Rev. Comput. Mol. Sci.*, 2022, **12**, e1606.
20. F. Weigend, *Phys. Chem. Chem. Phys.*, 2006, **8**, 1057–1065.
21. F. Weigend and R. Ahlrichs, *Phys. Chem. Chem. Phys.*, 2005, **7**, 3297–3305.
22. A. D. Becke, *The Journal of Chemical Physics*, 1993, **98**, 5648–5652.
23. C. Lee, W. Yang and R. G. Parr, *Phys. Rev. B*, 1988, **37**, 785–789.
24. P. J. Stephens, F. J. Devlin, C. F. Chabalowski and M. J. Frisch, *J. Phys. Chem.*, 1994, **98**, 11623–11627.
25. S. H. Vosko, L. Wilk and M. Nusair, *Can. J. Phys.*, 1980, **58**, 1200–1211.
26. J. W. Furness, A. D. Kaplan, J. Ning, J. P. Perdew and J. Sun, *J. Phys. Chem. Lett.*, 2020, **11**, 8208–8215.
27. Y. Zhao and D. G. Truhlar, *Theor. Chem. Acc.*, 2008, **120**, 215–241.
28. N. Mardirossian and M. Head-Gordon, *Phys. Chem. Chem. Phys.*, 2014, **16**, 9904–9924.
29. J. P. Perdew, *Phys. Rev. B*, 1986, **33**, 8822–8824.
30. J. P. Perdew, K. Burke and M. Ernzerhof, *Phys. Rev. Lett.*, 1997, **78**, 1396–1396.
31. M. Ernzerhof and J. P. Perdew, *J. Chem. Phys.*, 1998, **109**, 3313–3320.
32. H. S. Yu, X. He and D. G. Truhlar, *J. Chem. Theory Comput.*, 2016, **12**, 1280–1293.
33. Y. Zhao, N. E. Schultz and D. G. Truhlar, *J. Chem. Phys.*, 2005, **123**, 161103.
34. Y. Zhao, N. E. Schultz and D. G. Truhlar, *J. Chem. Theory Comput.*, 2006, **2**, 364–382.
35. H. S. Yu, X. He, S. L. Li and D. G. Truhlar, *Chem. Sci.*, 2016, **7**, 5032–5051.
36. V. N. Staroverov, G. E. Scuseria, J. Tao and J. P. Perdew, *J. Chem. Phys.*, 2004, **121**, 11507–11507.
37. A. J. Cohen and N. C. Handy, *Mol. Phys.*, 2001, **99**, 607–615.
38. F. Neese, A. Hansen and D. G. Liakos, *J. Chem. Phys.*, 2009, **131**, 064103.
39. F. Neese, F. Wennmohs and A. Hansen, *J. Chem. Phys.*, 2009, **130**, 114108.
40. S. Kossmann and F. Neese, *Journal of Chemical Theory and Computation*, 2010, **6**, 2325–2338.
41. C. Riplinger and F. Neese, *J. Chem. Phys.*, 2013, **138**, 034106.
42. C. Riplinger, B. Sandhoefer, A. Hansen and F. Neese, *J. Chem. Phys.*, 2013, **139**, 134101.

43. C. Riplinger, P. Pinski, U. Becker, E. F. Valeev and F. Neese, *J. Chem. Phys.*, 2016, **144**, 024109.
44. G. Bistoni, C. Riplinger, Y. Minenkov, L. Cavallo, A. A. Auer and F. Neese, *J. Chem. Theory Comput.*, 2017, **13**, 3220–3227.
45. M. Saitow, U. Becker, C. Riplinger, E. F. Valeev and F. Neese, *J. Chem. Phys.*, 2017, **146**, 164105.
46. B. Helmich-Paris, B. de Souza, F. Neese and R. Izsák, *J. Chem. Phys.*, 2021, **155**, 104109.
47. F. Neese, *J. Comput. Chem.*, 2023, **44**, 381–396.
48. T. H. Dunning, Jr., *J. Chem. Phys.*, 1989, **90**, 1007–1023.
49. M. Drosou, C. A. Mitsopoulou and D. A. Pantazis, *Polyhedron*, 2021, **208**, 115399.
50. Y. Guo, K. Sivalingam, E. F. Valeev and F. Neese, *J. Chem. Phys.*, 2016, **144**, 094111.
51. C. Kollmar, K. Sivalingam, B. Helmich-Paris, C. Angeli and F. Neese, *J. Comput. Chem.*, 2019, **40**, 1463–1470.
52. M. Ugandi and M. Roemelt, *Int. J. Quantum Chem*, 2023, **123**, e27045.
53. T. Lu and Q. Chen, *J. Phys. Chem. A*, 2023, **127**, 7023–7035.
54. M. J. Frisch, G. W. Trucks, H. B. Schlegel, G. E. Scuseria, M. A. Robb, J. R. Cheeseman, G. Scalmani, V. Barone, G. A. Petersson, H. Nakatsuji, X. Li, M. Caricato, A. V. Marenich, J. Bloino, B. G. Janesko, R. Gomperts, B. Mennucci, H. P. Hratchian, J. V. Ortiz, A. F. Izmaylov, J. L. Sonnenberg, Williams, F. Ding, F. Lipparini, F. Egidi, J. Goings, B. Peng, A. Petrone, T. Henderson, D. Ranasinghe, V. G. Zakrzewski, J. Gao, N. Rega, G. Zheng, W. Liang, M. Hada, M. Ehara, K. Toyota, R. Fukuda, J. Hasegawa, M. Ishida, T. Nakajima, Y. Honda, O. Kitao, H. Nakai, T. Vreven, K. Throssell, J. A. Montgomery Jr., J. E. Peralta, F. Ogliaro, M. J. Bearpark, J. J. Heyd, E. N. Brothers, K. N. Kudin, V. N. Staroverov, T. A. Keith, R. Kobayashi, J. Normand, K. Raghavachari, A. P. Rendell, J. C. Burant, S. S. Iyengar, J. Tomasi, M. Cossi, J. M. Millam, M. Klene, C. Adamo, R. Cammi, J. W. Ochterski, R. L. Martin, K. Morokuma, O. Farkas, J. B. Foresman and D. J. Fox, Gaussian, Inc., Wallingford, CT, 2016.
55. T. Lu, *J. Chem. Phys.*, 2024, **161**, 082503.
56. T. Lu and F. Chen, *J. Comput. Chem.*, 2012, **33**, 580–592.
57. M. P. Mitoraj, A. Michalak and T. Ziegler, *J. Chem. Theory Comput.*, 2009, **5**, 962–975.
58. A. Altun, F. Neese and G. Bistoni, *J. Chem. Theory Comput.*, 2019, **15**, 215–228.
59. E. C. Meng, T. D. Goddard, E. F. Pettersen, G. S. Couch, Z. J. Pearson, J. H. Morris and T. E. Ferrin, *Protein Sci.*, 2023, **32**, e4792.